applied sciences

MDPI

Article

Intensification of Dihydroxybenzenes Degradation over Immobilized TiO_2 Based Photocatalysts under Simulated Solar Light

Szymon Malinowski [1], Ivana Presečki [2], Igor Jajčinović [3], Ivan Brnardić [3], Vilko Mandić [4] and Ivana Grčić [2,*]

1 Faculty of Civil Engineering and Architecture, Lublin University of Technology, Nadbystrzycka 40, PL-20618 Lublin, Poland; s.malinowski@pollub.pl
2 Faculty of Geotechnical Engineering, University of Zagreb, Hallerova Aleja 7, HR-42000 Varaždin, Croatia; ivana.presecki@gfv.unizg.hr
3 Faculty of Metallurgy, University of Zagreb, Aleja Narodnih Heroja 3, HR-44000 Sisak, Croatia; jajcinovic@simet.hr (I.J.); brnardic@simet.hr (I.B.)
4 Faculty of Chemical Engineering and Technology, University of Zagreb, Marulićev trg 19, HR-10000 Zagreb, Croatia; vmandic@fkit.hr
* Correspondence: ivana.grcic@gfv.unizg.hr; Tel.: +385-42-408-945

Received: 27 September 2020; Accepted: 26 October 2020; Published: 27 October 2020

Featured Application: Solar photocatalysis is a promising technology of water purification for real scale applications. Intensification choices are readily available and mostly focused on optimal reactor design and/or effective photocatalyst formulation. Our study gives a simple methodology for the quantification of intensification potential, given that intensification indices are applicative in further research, simulations and predictions of degradation extents in various photocatalytic systems.

Abstract: The work is focused on the assessment of possible methods for intensification of photocatalytic degradation of common water borne pollutants. Solar photocatalysis poses certain limitations for large scale application with several possible reactor designs which have shown an optimal performance. In the current study, a comparison between two types of pilot scale reactors was made: a flat-plate cascade reactor (FPCR) and tubular reactor with a compound parabolic collector (CPC). Apart from the reactor design, another aspect of possible intensification was a photocatalyst formulation. The efficiency of photocatalytic films that consisted of pure TiO_2 nanoparticles was compared to the efficiency of films that consisted of TiO_2/CNT composites. Intensification assessment was performed via detailed kinetic modelling, combining the optical properties of films, irradiation conditions and reactor mass balance. Intensification was expressed via intensification indices. Results showed the advantage of the CPC-based reactor design and an unbiased effect of sensitizing agent (CNT) in the photocatalytic film formulation.

Keywords: TiO_2 films; TiO_2/CNT composites; photocatalysis kinetics; intensification index

1. Introduction

Industry development is mainly responsible for the introduction of a large volume of wastewater containing phenols into the environment. The phenolic compounds are one of the hugest groups of [1] toxic and corrosive [2] environmental pollutants released from various manufacturing industries, causing many environmental and toxicological problems [3]. The dihydroxybenzene isomers—i.e., catechol (CT), hydroquinone (HQ) and resorcinol (RS)—are common phenol-based compounds. These compounds are characterized by similar physicochemical properties and different locations of the two hydroxyl

groups [4,5]. The CT can be introduced into the environment from both anthropogenic—i.e., cosmetics, pharmaceutical or antioxidant industry—as well as natural sources—i.e., decomposition of humic and lignocellulosic substances [3,6]. The RS (1,3-dihydroxybenzene) found many applications in dyes, plastic and synthetic fiber production, whereas HQ (1,4-dihydroxybenzene) is widely employed as an industrial solvent [6] and found application in photography and cosmetics for skin pathologies treatment [7]. The existence and co-existence of dihydroxybenzene isomers in nature is a serious hazard to biological systems and the ecological environment [8]. Dihydroxybenzene isomers can enter the human body through mucous membranes, skin [9] and the gastrointestinal tract [10] causing poisoning symptoms and sometimes also headache, pale, dizziness, tiredness or even liver and kidney function damage [9]. In addition, Bukowska et al. [11] showed higher catechol toxicity compared to phenol because it damages erythrocytes functions at a 5-times lower concentration (50g/L for catechol, 250 g/L for phenol). A combination of their capacity accumulation in the environment [12]; low degradability level; and high toxicity for humans, animals and plants caused CT, HQ and RS to be considered as important environmental pollutants by the US Environmental Protection Agency (EPA) and European Union (EU) [3,13]. Due to carcinogenicity of dihydroxybenzene isomers even at low concentrations, they are considered as priority pollutants [14].

Due to the complex and stable chemical structure of phenolic pollutants, for their removal from aqueous solution, many conventional (i.e., steam distillation, liquid-liquid extraction, adsorption, solid-phase extraction, wet air oxidation, catalytic wet air oxidation, biodegradation) as well as advanced techniques (i.e., electrochemical oxidation, photo-oxidation, ozonation, UV/H_2O_2, Fenton reaction, membrane processes and enzymatic treatment) can be applied [15]. Among the conventional methods, adsorption of phenolic compounds [12] using different adsorbents—i.e., commercial and synthetic activated carbons [16–19], synthetic resins [20,21], zeolites, industrial waste/by-products i.e., coal [22], fly ash [23], red mud [14,24] and waste sludge [25,26]—is the most popular technique. The phenolic compound adsorption uses the fundamental interaction of aromatic rings [17] with adsorbent. However, its practical application has some disadvantages related to regeneration and high cost manufacturing of adsorbent [22]. Moreover, the use of adsorption also causes problems with the storage of the adsorbent containing adsorbed phenolic contaminants. Therefore, for several years, an increase in the use of Advanced Oxidation Processes (AOP_s) in wastewater treatment containing phenols has been observed. [27]. Among AOP_s is photocatalysis, which emerged in the 1980s. The definition of photocatalysis is still unclear, but usually this process is defined as a chemical reaction induced by photon absorption of a solid material (photocatalyst) which does not undergo chemical changes [28]. In the literature terms, photocatalyst and catalyst are used interchangeably because photocatalytic materials are sometimes used in catalysis. The clear difference between photocatalyst and catalyst terms is seen in terms of thermodynamics. During photocatalytic and catalytic reactions, Gibbs free enthalpy is positive ($\Delta G > 0$) and negative ($\Delta G < 0$), respectively [29]. In general, the photocatalytic process involves five subsequent steps: (1) pollutants transfer to photocatalyst surface, (2) adsorption of pollutants on the surface, (3) photonic activation and decomposition of adsorbed molecule, (4) reaction product's desorption and (5) removal of reaction products from the photocatalyst surface [30]. According to widely accepted theory, the base of the photocatalytic process is generation of electron-hole pairs on the photocatalyst surface as a result of the light with equal or higher energy than the energy gap of the photocatalyst. The formed electron-hole pairs dissociate into electrons in conduction band and holes in the valance band responsible for oxidation and reduction of adsorbed pollutants on photocatalyst surface [31]. Due to high effectiveness photocatalysis depending on photocatalytic activity of catalyst, light intensity and wavelength, dihydroxybenzene isomers' initial concentration, medium pH and co-existing substances [32], this process found many applications in phenolic compound degradation using many materials—i.e., Au-ZnO [33], TiO_2 [34,35], ZnO [36], TiO_2/graphene/heteropoly acid nanocomposite [37] or MnOx/TiO_2 nanocomposite [38]. It is reported that the modification with CNT enhanced the photocatalytic performance of CNT-TiO_2, Ag_3PO_4/CNT, CNT/g-C_3N_4, BiOI/CNT and Au@CNT@TiO_2 composites [39–43], as well as TiO_2/CNT anodes for H_2 generation [44].

The main aim of this work was to explore the aspects of the solar photocatalysis process intensification in optimal pilot scale reactor geometries. The solar photocatalysis is a surface phenomenon, highly dependent on the irradiation intensity reaching photocatalyst surface. In that manner, one way to intensify the process is the proper reactor design. This process can be conducted efficiently in some rather simple reactor configurations such as flat-plate reactor types. However, the use of compound parabolic collector (CPC)-based photoreactors is highly recommended by many researchers [45,46] since the light capture in reaction space is better than in flat-plate systems. The CPC-based configuration assumes closed tubular reactors, whereby in the case of slurry TiO_2 applications, incident light concentrated inside the tube may be utilized all over its diameter. The novelty presented in current study includes the use of immobilized photocatalyst inside the tube where it is fully exposed to incident irradiation; the goal was to estimate the intensification in comparison with a flat-plate cascade reactor (FPCR). Another method of intensification is the intervention in photocatalyst formulation to shift the absorption to the visible region and lower the energy gap. The latter is extensively investigated among researchers worldwide. However, a need for large scale immobilized photocatalysts for flat-plate reactors may limit the use of numerous doped TiO_2 due to price and small-scale production methods (e.g., anodization). In the current study, only commercially available components were used; TiO_2-based film made from TiO_2 P25 was modified by the addition of multi-walled carbon nanotubes (MWCNT). The photocatalytic film is simple to prepare ensuring the profitability of full-scale solar photocatalysis.

The highlight of the study was the simple methodology for quantitative estimation of solar photocatalysis intensification. Intensification indices were calculated via kinetic modeling, and the results were presented. The applied modeling allows a clearly comparison of different photocatalyst and reaction geometries as was shown in previous work [46,47]. Used kinetic models consisted of an irradiation term that quantified the effect of photocatalyst optical properties (i.e., irradiation absorption) and incident irradiation in both the UVA and UVB region on degradation of selected pollutants in water. Modelled parameters were intrinsic reaction rate constants for each studied compound and intensification indices related to reactor design or photocatalyst modification. The full methodology for the quantification of photocatalysis intensification is given.

2. Materials and Methods

2.1. Reaction Set-Up

The experiment was carried out in two different pilot scale reactors: flat-plate cascade reactor (FPCR) and tubular reactor with a compound parabolic collector (CPC), shown in Figure 1a,b. The FPCR (Figure 1a) consists of three cascades (500 × 250 mm) made from resistant polycarbonate material. Model solution was continuously recirculated from the collecting tank over cascades using a Masterflex peristaltic pump; flow was set at 8.0 cm^3/s. Total volume of model solution in recirculation was 1.7 dm^3. Water layer depth (h) over photocatalytic film was 0.7 ± 0.1 cm. The CPC reactor (Figure 1b) consists of two parallel quartz tubes (L = 500 mm, D_{outer} = 30 mm, D_{inner} = 27 mm), placed in the middle of a compound parabolic mirror made of highly reflective alumina (JBL Solar Reflect 50). Tubes were connected by a PTFE U-tube of the same internal diameter to avoid changes in model solution flow rates. Experiments were performed in total recirculation (Q = 26.5 cm^3/s), with a total volume of 1.5 dm^3 and effective reactor volume of 0.5 dm^3.

The irradiation source was a custom-made panel composed of three pairs of full-spectra lamps (JBL, Neuhofen, Germany, Solar Ultra linear fluorescent lamps, types: Color, Tropic and Natur; T5, 1450 mm, nominal power 80 W) placed in the reflective mirrors (JBL, Neuhofen, Germany, Solar Reflect 146) (Figure 1c). The distance between the FPCR cascade surface and the center of the lamps was 7 cm at the inlet (x_{max}) and 2 cm at the outlet position (x_{min}) to match the cascade length and the effective lamp length. In the case of CPC, both the panel and the tubes were inclined at 12°. The distance between the lamps and the top of the quartz tubes was adjusted to achieve the same

intensities as measured at the center of the FPCR cascade. The UVB and UVA intensities on the lamp wall (I_w) were determined radiometrically using the UVX radiometer fitted with a corresponding midrange UV-B UVX-31 (range 280–340 nm) and longwave UV-A UVX-36 sensor (range 335-385 nm) with a sensor accuracy of ± 5% (UVP Products, Analytik Jena US LLC, Upland, CA). The obtained average UVB and UVA intensities will be discussed later.

In a typical experiment, model solution recirculated over the photocatalyst in the dark for 30 min before irradiation started to achieve sorption equilibrium. The photocatalytic process lasted 180 min. Control experiments were performed in the dark to estimate the adsorption of model compounds on the photocatalytic film or possible "dark" catalysis in the full length of 180 min. Additionally, model solutions were recirculated in empty reactors (without photocatalyst) under given irradiation conditions to exclude the effects of direct photolysis on overall degradation rates. All experiments were performed at least twice, and average values were reported.

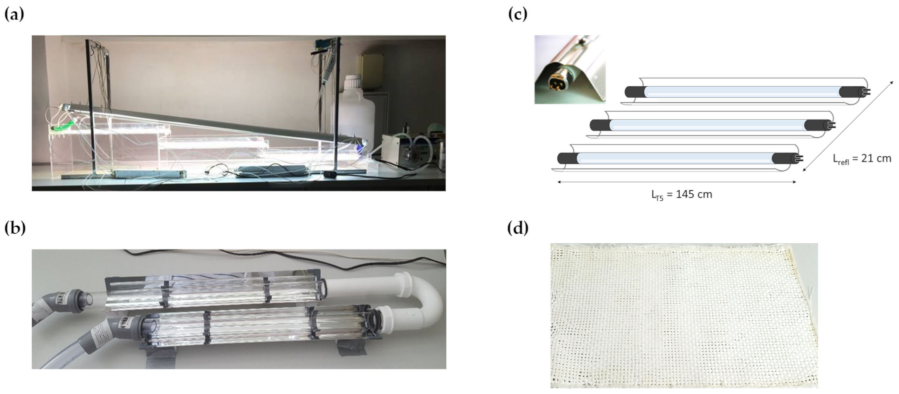

Figure 1. (**a**) The flat-plate cascade reactor (FPCR) reactor; (**b**) the compound parabolic collector (CPC) reactor; (**c**) schematics of custom-made panel with linear fluorescent lamps; (**d**) the image of photocatalyst-TiO_2 photocatalytic film on glass fiber mesh (TiO_2-GF).

2.2. Model Pollutants

In this work, the photocatalytic degradation of dihydroxybenzenes: catechol (CT), hydroquinone (HQ) and resorcinol (RS) was studied. Single model solutions of CT, HQ and RS (all p.a., Fluka) were prepared with the initial concentration of 100 µmol/L. In addition, binary mixtures were made: CT+HQ, CT+RS and HQ+RS with the same concentration of a single compound.

Concentration of each compound was determined using high performance liquid chromatography (HPLC, Knauer, Berlin, Germany) with a UV absorbance detector. The column used for separation of these compounds was Supelco C-18. The levels of quantification for studied compounds were 1.0×10^{-6} mol/L. The analyses were carried out by binary flow elution with mobile phase solvents A and B at a flow rate of 0.6 and 0.4 mL/min, respectively. Solvent A consisted of 0.5:99.5 (*v*/*v*) methanol: 0.1 M phosphoric acid, and solvent B was 100% methanol. The CT, HQ and RS were quantified at 276, 288 and 272 nm.

2.3. Photocatalytic Films

The photocatalyst was immobilized on the surface of a glass fiber mesh—i.e., a roving fabric made completely from glass fibers (density 480 g/m^2) (Figure 1d). Support was cut into exact dimensions prior to photocatalysts immobilization: 480 × 250 mm. Immobilization was performed using the modified sol-gel procedure described previously in [48–50]. The TiO_2 (Evonik, Aeroxide®, TiO_2 P25; with an elementary particle size of 30 nm, BET surface area of 56 m^2/g and crystalline content of 75% anatase and 25% rutile); acetic acid (Kemika); tetraetoxysilane (TEOS) (Aldrich Chemicals); ethanol p.a., 96%; deionized water; and 10M NaOH were used. The solution for immobilization of water, ethanol and TiO_2 with the use of acetic acid for adjusting pH value at 1.5 was mixed for 15 min. After mixing,

sonication of the solution was performed with the ultrasonic probe for 2 min (30 W, frequency 20 kHz). Furthermore, TEOS was added, and mixing at 50 °C continued for 1 h. Before the immobilization, glass fiber mesh supports were cleaned with the ethanol, treated with 10M NaOH for 5 min and washed with deionized water. Immobilization was performed through the dipping of supports in prepared solution and dried for 15 min on 70 °C, repeatedly 4 times. Films made of TiO_2 was marked as TiO_2-GF. The image of immobilized photocatalysts (TiO_2-GF) is given in Figure 1d. To study the intensification due to sensitization by carbon nanotubes (MWCNT, Sigma, 50–90 nm diameter, >95% carbon basis), another film series was made using TiO_2 and CNT (10:1, w:w), marked as TiO_2/CNT-GF.

The characterization was performed using different techniques. The Raman spectroscopy measurements were performed using a HORIBA Jobin Yvon T64000 spectrometer with a 532.5 nm solid-state laser excitation. The spectra were collected in micro-Raman mode with a multi-channel CCD detector, laser power of 20 mW at the sample and an objective with a 50× magnification (Olympus) in a spectral range of 100–3000 cm^{-1}.

The scanning electron microscopy (SEM) was performed with scanning electron microscopy (SEM) by an FEG SEM Quanta 250 FEI microscope operating at 20 kV and working distance set at 20 mm. The samples for SEM characterization were prepared by placing carriers on a sample holder covered with a piece of double-sided carbon conductive tape and then coated with the Au-Pt.

The UV-VIS spectra of the prepared powder samples were obtained using diffuse reflectance spectroscopy (DRS) on a Perkin-Elmer Lambda 35 device equipped with an integrating sphere. The spectra were recorded at room temperature in the wavelength range of 200–800 nm. The $BaSO_4$ and Spectralon were used as a reference. The diffuse reflectance spectra were transformed by performing a Kubelka-Munk transformation of the measured reflectance according to: $F(R) = (1 - R^2)/2R$, where F(R) is proportional to the extinction coefficient (α) and R is the reflectance of the "infinitely thick" layer of the solid. The bandgap energy, Eg, was estimated by plotting the modified Kubelka-Munk function, $(F(R)h\nu)^n$, vs. photon energy ($h\nu$), the Tauc plot, followed by extrapolation of the linear region of high slope region onto the energy axis. In the modified Kubelka-Munk function, h is Planck's constant and ν is frequency; the exponent n is associated with electronic transition in the course of the optical absorption process. The exponent n is theoretically equal to 1/2 and 2 for indirect and direct allowed transitions, respectively. The exponent n is theoretically equal to 1/3 and 2/3 for indirect and direct forbidden transitions, respectively [51].

3. Results and Discussion

3.1. Intensification by Reactor Design

Our recent studies showed that the incident photon flux at the surface of the reactor or photocatalytic film facing the lamps in FPCR can be calculated with the Extensive Source Superficial Diffuse Emission (ESSDE) model [49]. Due to the angular position of the panel with respect to the cascade surface, variations along the cascade axial direction (H) are expected, while the incident irradiation on a single point of the FPCR surface varies also in respect to the distance from the lamp center. In the current study, average values of the incident photon flux at the surface of the photocatalytic film (I_0, mW/cm^2) were determined using radiometric readings before and during experiments at different positions along the photocatalyst surface. As shown in Figure 2, the mean I_0 intensities in FPCR (Figure 2a) are a result of a combination of irradiation emissions from used lamps (Figure 2b) and correspond well to the irradiation conditions during cloudy to partially sunny days in winter and early spring in Zagreb, Croatia (45°N). The UVB and UVA irradiance levels at the given location were obtained from the radiometric readings on horizontal surface. The use of those lamps allowed different UVA and UVB intensities in reaction space (Figure 2a,b), which is a close simulation of natural sunlight, whereby intensity levels depend not only on the time of the day and a season but also on the cloudiness. As shown in Figure 2a, the irradiated surface was divided into

areas in i.e., distinct UV regions. The exact UVB and UVA intensities were used in the kinetic models, which resulted in reliable parameters that were confirmed in all experiments.

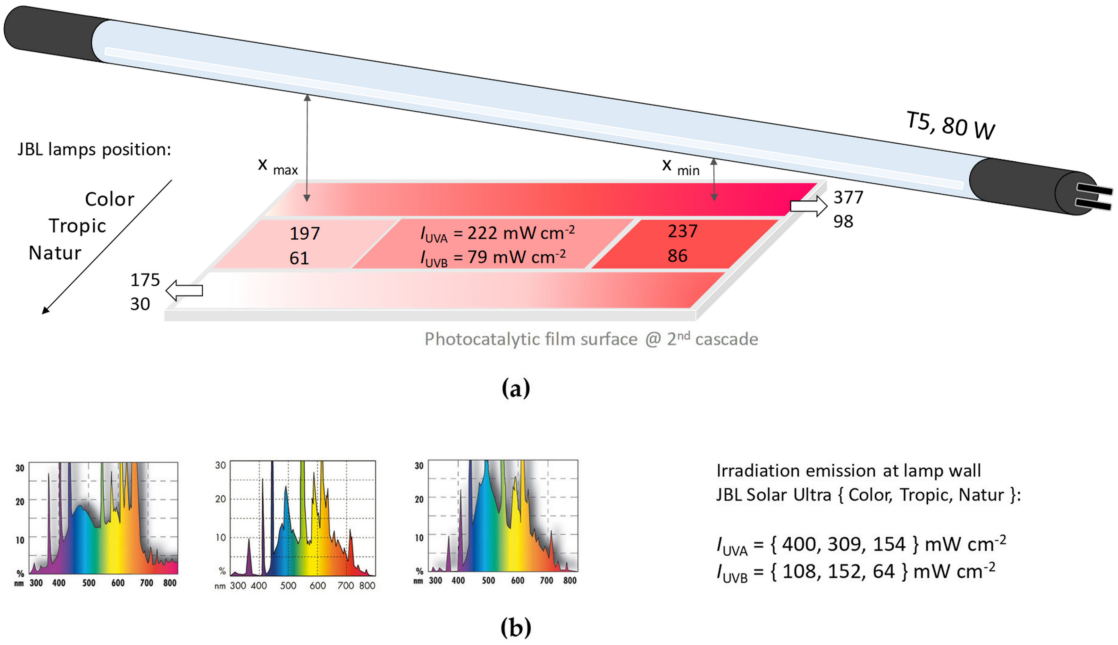

Figure 2. (**a**) Average incident irradiation intensities on photocatalyst surface in regard to lamps' positioning (measurements at 2nd cascade of FPCR were given as an example); (**b**) lamps' emission spectra as obtained by the manufacturer (JBL).

In CPC, total irradiation in the quartz tubes is the sum of the incident irradiation—i.e., direct and diffuse irradiation coming from the lamps—and reflected radiation coming from the parabolic mirrors. Snell's law of specular materials can be used to estimate the flux loss of the reflected radiation reaching the reactor, Equation (1)

$$I_{\text{refl}} = I_{0,\text{total}} \Psi^{g} \quad (1)$$

where I_0 is the incident solar radiation flux reaching the reactor walls, Ψ is the material reflectivity and g is the number of consecutive reflections of the ray on the involute surface [45]. In the current study, the main hypothesis is the intensification of the photocatalytic process due to the CPC design, caused by the addition of reflected radiation and higher UVB and UVA intensities inside the quartz tubes. In that manner, the reflected irradiation was not calculated, but the same incident solar irradiation flux (I_0) was used for FPCR and CPC reactors. The difference in actual incident irradiation inside the CPC and used I_0 is proportional to intensification index, since only better light capture is responsible for intensification. The corresponding intensification index will be calculated later on.

The photocatalytic degradation of CT, HQ and RS and binary mixtures was performed in both the FPCR and CPC reactor, and the results are given in Figure 3a–c. In both reactors, direct photolysis of CT, HQ and RS or the respective adsorption on TiO_2-GF in the dark was negligible during 180 min of the control experiment. Results from control experiments also excluded any effect of dark catalytic reactions on pollutant degradation during the solar photocatalytic process under given circumstances (data not shown).

As shown in Figure 3, the obtained results show the similar kinetic trends, with faster degradation in CPC. The extent of CT degradation in FPCR over irradiated TiO_2-GF film reached 46%, while degradation in CPC reached 63% after 180 min of treatment. The degradation extents of HQ were 58% and 78% in FPCR and CPC, respectively. The degradation extents of RS were 56% and 71% in FPCR and CPC, respectively. Similar observations were made for CT, HQ and RS degradation in binary mixtures.

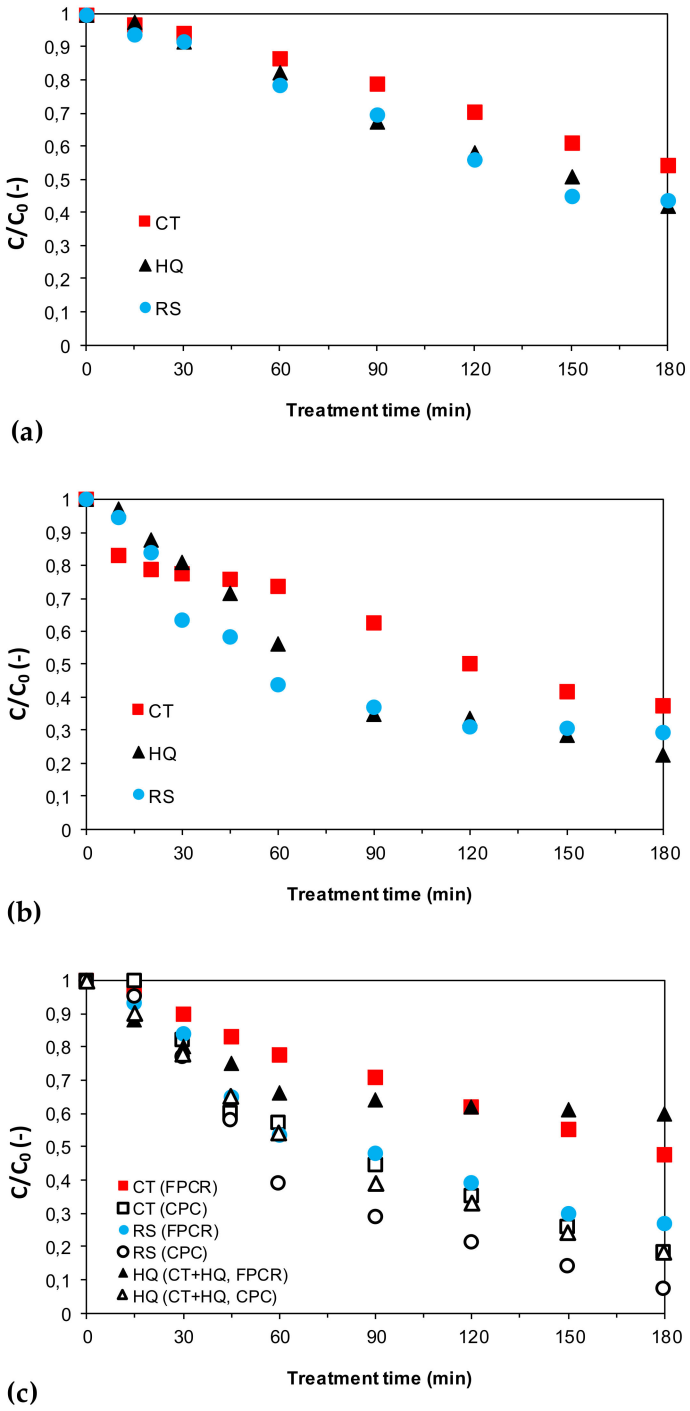

Figure 3. Normalized concentration profiles of dihydroxybenzenes during photocatalytic experiments using TiO_2-GF: (**a**) degradation of CT, HQ and RS in single pollutant model solutions in FPCR at given experimental conditions; (**b**) degradation of CT, HQ and RS in single pollutant model solutions in CPC at given experimental conditions; (**c**) degradation of CT (red and white squares) and RS (blue and white circles in CT+RS binary mixture in FPCR and CPC and degradation of HQ (triangles) in CT+HQ binary mixture in FPCRC and CPC at given experimental conditions.

Having in mind different hydrodynamics and mean residence time, these results need to be properly managed by detailed kinetic modeling prior to final conclusion regarding the degradation efficiency and possibility of intensification using CPC reactors.

3.2. Intensification by Photocatalyst Formulation

Following Micro-Raman spectroscopy, a sample of pure MWCNT (C) showed the characteristic G, D peak and 2D (or G') bands (second-order two-phonon process), at 1340, 1580 and 2680 cm^{-1}, characteristic for carbon nanotubes, indicating stacking order (Figure 4). Glass fiber mesh alone does not show Raman bands (not shown). Titania sample (T) showed bands characteristic for TiO_2 at 148, 286, 399 and 633 cm^{-1} assigned to anatase, with a very weak band at 286 cm^{-1}, possibly belonging to the rutile second order process [52]. Basically, TiO_2 bands dominate the composite sample (TiO_2/CNT-GF). For TiO_2/CNT-GF, sample bands related to MWCNT (D band and G band) are affected and appear at 1290 and 1620 cm^{-1}. A new band was observed at 1730 cm^{-1} due to rearrangement of carbonaceous bonding due to specific MWCNT to mesh surface bonding (Figure 4a). The appearance of the band at 1730 cm^{-1} is quite indicative in terms of achieving chemical bonds between the constituents in the TiO_2/CNT-GF sample. In order to determine the bonding of the TiO_2 and MWCNT immobilized on fiber glass mesh, SEM analysis with different magnifications was performed on the TiO_2/CNT-GF sample (Figure 4b).

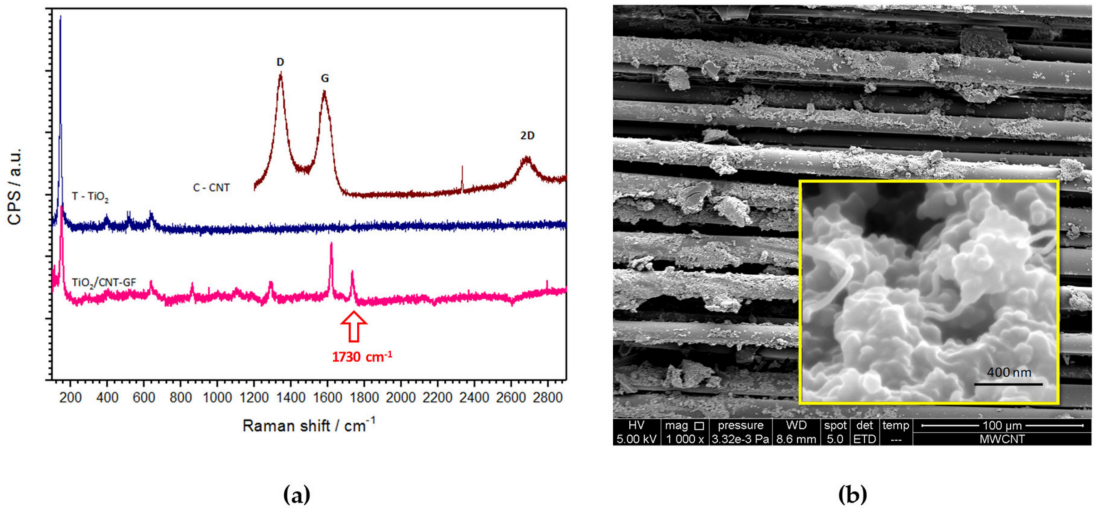

(a) **(b)**

Figure 4. (**a**) Raman spectra of the photocatalytic constituents and composite film on glass fiber mesh; (**b**) SEM image of TiO_2/CNT-GF at 1000 magnification and 200,000× (given as embedded figure).

From the SEM results, it can be seen that a successful immobilization of TiO_2 and MWCNT on carriers occurred. Note that immobilization is not uniform: some parts of fibers are coated with TiO_2/CNT aggregates, while others appeared clean. However, they were still coated with nanoparticles along the whole length, which can be seen by detailed analysis of higher magnifications (results not shown). As shown in the embedded figure, bonding of TiO_2 and MWCNT is clearly observed at higher magnification (200,000×), which is in correlation with the presumption given from Raman spectra.

The DRS spectra of the samples clearly depict differences. From Figure 5a, one can observe that all samples exhibit photoabsorption in the range between 250 and 400 nm. The Kubelka-Munk function was applied to relatively enhance the absorption bands of different samples of photocatalytic films. Generally, different types of constituents display different behavior: e.g., MWCNT absorption is characteristic for conducting materials, while TiO_2 absorption is characteristic for semiconducting materials. In order to evaluate the type of transitions, extent of transitions and bandgaps for derived composite samples (with respect to the constituents), the Tauc equation was applied (Figure 5b). Namely, anatase is an unquestionably semiconducting material, and it is widely accepted as it undergoes indirect allowed transitions (n = 1/2) (bandgap near the value of 3.2 eV). Other constituents are generally not semiconducting materials but may hinder or contribute to the semiconducting behavior of the composite. For that matter, they may be evaluated as semiconductors, although they are generally not semiconductors. Therefore, conventional calcium silicate glass undergoes indirect

allowed transitions (n = 1/2) (bandgap near the value of 3.85 eV). Among carbon-based substances, depending on the treatment, MWCNT shows direct allowed transitions (n = 2) (bandgap value from 2.9 to 3.6 eV). Bandgaps determined from the Tauc plot show 3.22 and 3.48 eV for pure TiO_2 (T) and glass-fibre (GF) constituents, respectively. For the composite sample, different transitions were tested, and those that dominate (best describe the sample optoelectric performance and photocatalytic behavior) were selected. For the TiO_2/CNT-GF sample, the situation is somewhat ambiguous. In the case of MWCNT governing the film behavior (direct allowed transitions in composites), the calculated bandgap value is 3.27 eV. In the case of anatase governing the film behavior (indirect allowed transitions), the calculated bandgap value is 2.97 eV. It seems that the none of the transition types fully dominate, hence the average bandgap value of approximately 3.12 eV may be expected. Those values suggest that a considerable synergetic photocatalytic effect was achieved by preparing the composite—i.e., boding of the carbonaceous species to titania species (confirmed by Raman) modifies the photoabsorption of the derived composites.

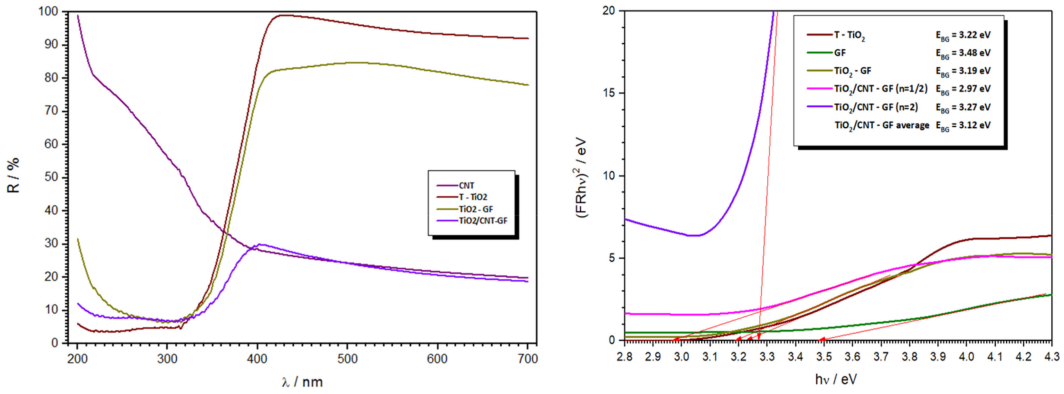

(a) **(b)**

Figure 5. (**a**) DRS UV-VIS spectra (**b**) Tauc plot for the photocatalytic film constituents and photocatalytic composites on glass mesh.

Experiments of CT, HQ and RS photocatalytic degradation were performed in FPCR using both TiO_2-GF and TiO_2/CNT-GF films. Results are given in Figure 6a,b. The results showed the higher degradation extents when photocatalytic films were modified with CNT, confirming the hypothesis of intensification by sensitization. The extent of CT degradation in FPCR over irradiated TiO_2-GF film reached 46%, while degradation over TiO_2/CNT-GF film reached 52% after 180 min of treatment. The degradation extents of RS over irradiated TiO_2-GF and TiO_2/CNT-GF films after 180 min of treatment in FPCR were 56% and 72%, respectively. The sensitization effect of CNT was different for HQ where 58% and 47% of degradation, respectively, were obtained after 180 min of treatment in FPCR over irradiated TiO_2-GF and TiO_2/CNT-GF films. The possible adsorption of HQ on CNT on the film surface via the -OH group in para position could produce certain steric disturbance for eventual •OH radical attack, which can explain the observed deviation and lack of sensitization effect in the case of HQ model solution.

The positive sensitization effects were observed for binary mixtures. CT and RS degradation kinetics are shown as observed in the CT+RS mixture, while HQ degradation is presented as an exemplary compound for the CT+HQ mixture in Figure 6b. The extent of CT degradation in the CT+RS mixture in FPCR over irradiated TiO_2-GF film reached 53%, while degradation over TiO_2/CNT-GF film reached 84% after 180 min of treatment. The degradation extents of RS over irradiated TiO_2-GF and TiO_2/CNT-GF films after 180 of treatment in FPCR were 73% and 96%, respectively. HQ degradation in CT+HQ mixture reached only 40% after 180 min of treatment, while sensitization of photocatalytic film led to 77% of HQ degradation. In general, dihydroxybenzenes degradation was faster in binary mixtures. With more of these substances on the photocatalyst surface, the pronounced hydroxylation,

ring openings and radical ejection could self-catalyze the radical cycle reactions as an underlying mechanism of photocatalytic degradation. In the absence of catalytic reactions in the dark, as confirmed in control experiments, it is evident that all radical cycle reactions are initiated by the •OH radical attack, formed on the surface of irradiated photocatalyst.

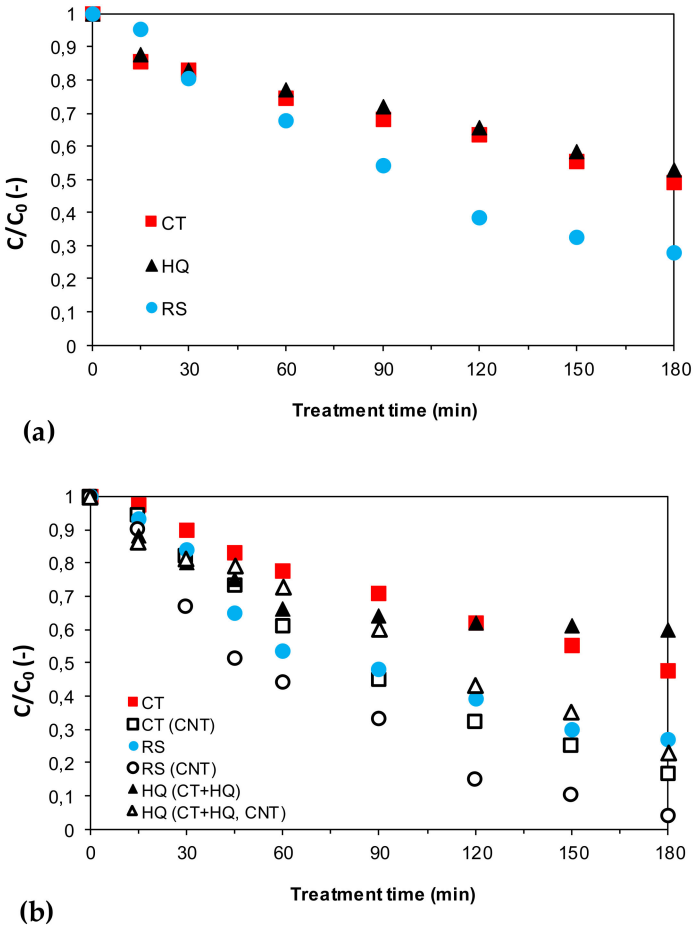

Figure 6. Normalized concentration profiles of dihydroxybenzenes during photocatalytic experiments in FPCR: (**a**) degradation of CT, HQ and RS in single pollutant model solutions using TiO_2/CNT-GF; (**b**) degradation of CT (red and white squares) and RS (blue and white circles in CT+RS binary mixture using TiO_2-GF and TiO_2/CNT-GF, and degradation of HQ (triangles) in CT+HQ binary mixture using TiO_2-GF and TiO_2/CNT-GF at given experimental conditions.

Control experiments showed that the adsorption equilibrium of CT, HQ and RS on TiO_2/CNT-GF was achieved in 10–15 min in the dark, and the respective concentration of each model pollutant remained the same afterwards. The adsorption of CT, HQ and RS on TiO_2/CNT-GF in the dark led to only 1.7%, 4.6% and 0.8 % initial concentration decrease, which is different than zero as in the case of TiO_2-GF but also negligible in terms of overall degradation extents.

The better photocatalytic performance of TiO_2/CNT composite can be explained by the formation of the Ti–O–C structure that can improve the transfer of photoinduced free electrons from TiO_2 to CNT, and overcome fast recombination of e-/h+ by formation of heterojunctions. Moreover, CNT increased the visible light absorption of composites, while the addition of CNT increased the specific surface area, thus serving as an optical support [39].

3.3. Calculation of Intensification Indices

To unbiasedly estimate the intensification possibility using different reactor designs and sensitized photocatalytic film, kinetics of photocatalytic degradation of model compounds in studied reactors must be properly modeled. The basic kinetic equation ($r = k\,[X]^n$) was firstly modified to give more intrinsic parameters related to photocatalytic degradation of selected pollutants over irradiated TiO_2 film. An irradiation term was introduced to basic kinetic equations:

$$r_i = -k_i\Big((\mu I_0(T,H))_{UVB} + (\mu I_0(T,H))_{UVA}\Big)^m [X_i]^n \quad (2)$$

The I_0(T,H) (W m^{-2}) stands for the incident photon flux at the film surface along the cascade width and length, μ (m^{-1}) is the absorption coefficient averaged over the spectrum of incident irradiation (in UVB and UVA region) and m is the order of reaction with respect to irradiation absorption. By introducing the (μI_0 (T,H))^m into the kinetic model, resulting reaction rate constants became independent of irradiation condition and applied catalyst [48]. Note that k_i stands for the intrinsic degradation rate constant of selected pollutants (i).

The intensification by reactor design was quantified using intensification index, Υ_{RD}.

$$r_i = -k_i\Big(\Upsilon_{RD}\Big((\mu I_0(T,H))_{UVB} + (\mu I_0(T,H))_{UVA}\Big)\Big)^m [X_i]^n \quad (3)$$

The intensification by photocatalyst formulation modification was quantified using intensification index, Υ_{cat}

$$r_i = -k_i\Upsilon_{cat}\Big((\mu I_0(T,H))_{UVB} + (\mu I_0(T,H))_{UVA}\Big)^m [X_i]^n \quad (4)$$

Note that Υ_{RD} multiplies the equation terms related to photon absorption rate, while Υ_{cat} multiplies the whole kinetic equation. The explanation is rather simple. In CPC, which is assumed as an optimal solar reactor design, irradiation conditions inside the reaction space are better than in FPCR, since the total incident irradiation is composed of incident irradiation at the reactor wall and reflected radiation. In that manner, Υ_{RD} represents the ratio between the total irradiation inside the reaction tubes and the incident irradiation at the outer reactor wall:

$$\Upsilon_{RD} = \frac{I_0(CPC)}{I_0(FPCR)} = \frac{I_0 + I_{refl}}{I_0} = 1 + \psi^g \quad (5)$$

Having in mind a variety of models [45,46] which can give the exact number of reflections (g) from collectors depending on the reactor inclination toward irradiation source, Υ_{RD} can be simply calculated from g and known material reflectivity (ψ), and introduced in different kinetic models. In another words, Υ_{RD} in this study was determined by semiempirical models, while it can be also calculated from different ray optics models. The predicted Υ_{RD} in CPC type reactors can lead to simple simulation of degradation extents for various pollutants and various hydrodynamic conditions, thus representing the solid base for scale up. The Υ_{cat} assumes the enhancement in light absorption by photocatalysts, both in the UVA and UVB region but also in the visible part of applied irradiation. It can be used for facile determination of total intensification for new improved photocatalyst formulations.

The reaction kinetic model was further combined with the material balance for plug flow reactor in recirculation. The Reynolds number was estimated using the hydraulic diameter equal to the wetted perimeter of a rectangular open channel (FPCR) and a pipe (CPC). Calculated Reynolds numbers for maintained flow in FPCR and CPC were 25.9 and 134.8, respectively. Despite the laminar flow, average velocity was used neglecting the radial and axial differences in the velocity profile. The averaged fluid velocity was estimated at $v = 2.78 \times 10^{-2}$ m/s in FPCR and $v = 4.99 \times 10^{-2}$ m/s in CPC, which was used in all related models. The PFCR operated in total recirculation mode with the reactor outlet flow entering the inlet with the minimum retention volume in the collecting tank. In CPC,

outlet flow mixed with the reaction mixture in the recirculation tank led to different inlet concentrations in different reaction times. Material balance is given for the perfectly mixed reservoir tank:

$$V_{\text{Tank}} \frac{d\,[\text{X}_\text{i}]^{\text{out}}_{\text{Tank}}}{\text{dt}} = Q\Big([\text{X}_\text{i}]^{\text{in}}_{\text{Tank}} - [\text{X}_\text{i}]^{\text{out}}_{\text{Tank}} \Big) \tag{6}$$

and for reactors CPC, Equation (7) and FPCR (single cascade), Equation (8):

$$v\frac{d[\text{X}_\text{i}]}{dH} = r_\text{i}(\text{H}, \text{t}) \tag{7}$$

$$v\frac{d[\text{X}_\text{i}]}{dH} = r_\text{i}(\text{H}, \text{T}, \text{t}) \tag{8}$$

The numerical simulation was performed dividing the reaction space along the length and width—i.e., H and T (in FPCR) directions—in sufficiently small intervals. A small time increment (Δt) equal to the reactor space time ($\tau = V_R/Q$) was introduced. The material balance in the reactor was solved at time t. The time step counter was increased and the procedure repeated. All simulations were performed in VBA module (Excel). Reaction rate constants (k_i, $\text{s}^{-1}\text{W}^{-0.5}\text{m}^{1.5}$) were determined by the trial and error method fitting the experimental values into the model by minimizing the variance.

The results are graphically represented in Figure 7a–f. All results show a good match between experimental data and applied mathematical models. Reaction rate constants (k_i, $\text{s}^{-1}\text{W}^{-0.5}\text{m}^{1.5}$) were determined from experimental data obtained from experiments in FCPR with TiO_2-GF (marked as "model FPCR"). k_i was kept constant in models applied to either FCPR with TiO_2/CNT-GF (model FPCR+Y_{cat}) or CPC (model CPC). If k_i for the specific pollutant deviated in any of these models, it would have suggested that the hypotheses were erroneous. However, the used *k*i values resulted in predicted model values for CT, HQ and RS concentration that match well with the corresponding experimental data. The use of the modified kinetic equation (Equation (1)) with irradiation terms allowed the determination of intrinsic kinetic rate constants that accurately describe the photocatalytic kinetics under variable UVA and UVB irradiation. Results of kinetic modelling and given intensification indices are given in Tables 1 and 2.

As shown in Table 1, observed reaction rate constants for CT, HQ and RS degradation in single pollutant model solutions were lower than the reaction rate constants for dihydroxybenzene degradation in binary mixtures. Although k_i is intrinsic value, specific for each pollutant, in such semiempirical models, it is a measure of reaction kinetics based on •OH radical attack and subsequent degradation mechanism. If any other reaction intervened the pollutant degradation, the k_i would change since it would be no longer a measure of simple photocatalytic kinetics. The observed phenomenon was explained in the previous section; faster degradation kinetics in the binary mixture is a result of the self-catalyzed radical reaction cycle due to a large number of hydroxyl-compounds on the photocatalyst surface. The results indicate a more rapid degradation of the single dihydroxybenzene compound in mixture, whereby the existence and activity of different short-lived radicals during the photocatalytic cycle overrides the possible negative effect of competitive adsorption on active sites and competitiveness toward reactive species. Again, the k_i values determined in the model for FPCR remained constant in the FPCR + Y_{cat} and CPC model, confirming the validity of presented semiempirical models.

The applied modelling approach assumed the calculations of Y_{RD} and Y_{cat} that are specific for upgraded reactor geometry and photocatalyst formulation enhancement, respectively. This means that calculated intensification indices should be the same in default settings. The uniformity of calculated Y_{RD} and Y_{cat} (Table 2) confirmed the validity of applied approach. The calculated intensification indices show a good match independent of the studied model solution. The Y_{RD} and Y_{cat} were found to be 6.77 and 1.64 with reasonably low standard deviation.

The value of Y_{RD} suggests that intensification by reactor design is the correct choice for optimization and further scale-up of reactors engaged in solar photocatalysis. Having in mind only 4.11% of available

UV irradiation from natural sunlight, the capture and multiplication of incident irradiation in the reaction space utilizing CPC-based reactors are general design goals. The Y_{cat} values suggested approximately 60% better photocatalytic efficiency due to the sensitization effect from CNT in film formulation.

Both intensification choices, either by reactor design or photocatalyst formulation, are necessary for real-scale solar photocatalysis applications. The presented methodology for calculation of intensification indexes is simple, robust and applicative in further research.

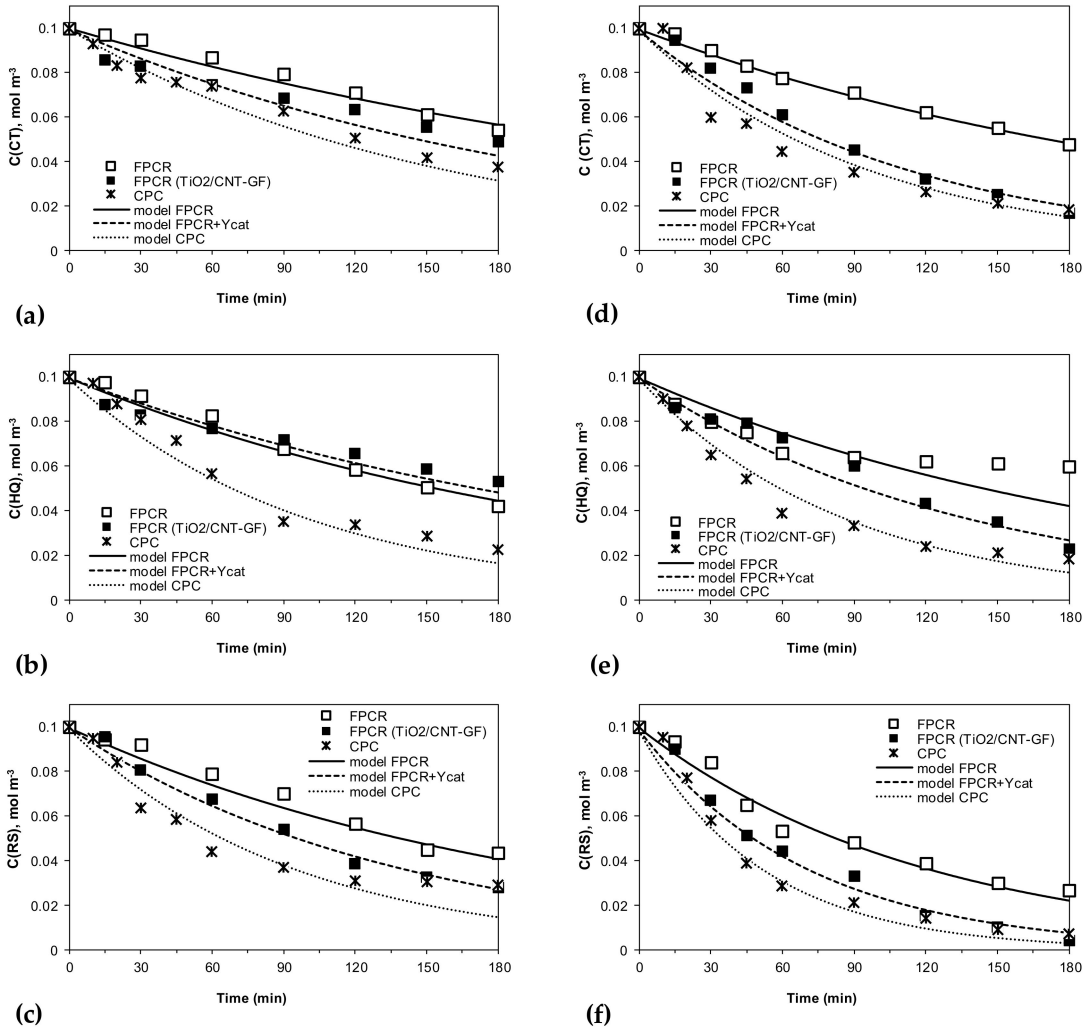

Figure 7. Comparison of experimental data and model values for degradation kinetics CT, HQ and RS in single pollutant model solutions (**a**–**c**) and binary mixtures (**d**–**f**) in FPCR and CPC using TiO_2-GF and TiO_2/CNT-GF (marked in legend). Models FPCR, FPCR+Y_{cat} and CPC relate to Equations (2)–(4), respectively.

Table 1. Kinetic model parameters.

Model Solution	CT	HQ	RS	CT+HQ	CT+RS	HQ+RS
k_i, $s^{-1}W^{-0.5}m^{1.5}$						
CT	3.1×10^{10}	-	-	4.0×10^{10}	4.1×10^{10}	-
HQ	-	4.4×10^{10}	-	4.7×10^{10}	-	4.7×10^{10}
RS	-	-	4.9×10^{10}	-	8.1×10^{10}	8.2×10^{10}
μ_{UVB}, m^{-1}	2.0×10^{7} [40]					
μ_{UVB}, m^{-1}	7.3×10^{6} [40]					

Table 2. Calculated intensification indices, Y_{RD} and $Y_{cat.}$

Model Solution	Y_{RD}	Y_{cat}
CT	5.99	1.50
HQ	6.50	0.90
RS	6.22	1.50
CT+HQ	7.10 (CT) 7.00 (HQ)	2.20 (CT) 1.64 (HQ)
CT+RS	6.90 (CT) 6.77 (RS)	1.75 (CT) 1.70 (RS)
HQ+RS	7.04 (HQ) 6.55 (RS)	1.75 (HQ) 1.49 (RS)
median	6.77 ± 0.39	1.64 ± 0.34

4. Conclusions

The study was focused on the quantification of photocatalytic degradation intensification. Two methods of intensification were studied: reactor design and photocatalysts formulation. A comparison of the two types of pilot scale reactors—flat-plate cascade and CPC-based—was given. The calculated intensification index due to the reactor design was around 6.7, giving the advantage to CPC-based reactors for solar photocatalytic. Sensitization of solar photocatalysis by the addition of carbon nanotubes to TiO_2 films led to intensification by 60%. Successful degradation of dihydroxybenzenes at low UV irradiation indicates the promising results of real-scale solar photocatalysis application in terms of environmental protection.

Author Contributions: Conceptualization, I.P., I.B. and I.G.; methodology, V.M. and I.G.; software, I.J. and I.G.; validation, S.M., V.M. and I.G.; formal analysis, S.M. and I.P.; investigation, S.M., I.J. and I.B.; resources, I.P., V.M. and I.G.; data curation, S.M., I.J. and V.M.; writing—original draft preparation, S.M., V.M. and I.G.; writing—review and editing, S.M., V.M., I.B. and I.G.; visualization, I.J., V.M., I.B. and I.G.; supervision, I.P.,I.B. and I.G.; project administration, I.G.; funding acquisition, V.M. and I.G. All authors have read and agreed to the published version of the manuscript.

Funding: This work has been supported by following projects "Waste & Sun for photocatalytic degradation of micropollutants in water" (OS-Mi), supported by European Regional Development Fund, KK.01.1.1.04.0006. (photocatalysts preparation and photocatalytic studies) and "PV-WALL" PZS-2019-02-1555 in the Research Cooperability Program of the Croatian Science Foundation funded by the European Union from the European Social Fund under the Operational Programme Efficient Human Resources 2014–2020 (material characterization).

Acknowledgments: S. Malinowski would like to thank the Cooperation of Science and Technology (COST) Action CA 16215 (PortASAP—European network for the promotion of portable, affordable and simple analytical platform), which supported the study visit in the frame of the STSM program.

Conflicts of Interest: The authors declare no conflict of interest.

References

1. Duan, W.; Meng, F.; Cui, H.; Lin, Y.; Wang, G.; Wu, J. Ecotoxicity of phenol and cresols to aquatic organisms: A review. *Ecotoxicol. Environ. Saf.* **2018**, *157*, 441–456. [PubMed]
2. Al Mamari, H.H.; Štefane, B.; Žugelj, H.B. Metal-catalyzed C–H bond functionalization of phenol derivatives. *Tetrahedron* **2020**, *76*, 130925.
3. Karami, C.; Taher, M.A. A catechol biosensor based on immobilizing laccase to Fe_3O_4@Au core-shell nanoparticles. *Int. J. Biol. Macromol.* **2019**, *129*, 84–90. [PubMed]
4. Zhang, H.; Huang, Y.; Hu, S.; Huang, Q.; Wei, C.; Zhang, W.; Yang, W.; Dong, P.; Hao, A. Self-assembly of graphitic carbon nitride nanosheets-carbon nanotube composite for electrochemical simultaneous determination of catechol and hydroquinone. *Electrochim. Acta* **2015**, *176*, 28–35.
5. Suresh, S.; Srivastava, V.C.; Mishra, I.M. Adsorption of catechol, resorcinol, hydroquinone and their Derivatives: A Review. *Int. J. Energy Environ. Eng.* **2012**, *3*, 1–19.
6. Maleki, N.; Kashanian, S.; Maleki, E.; Nazari, M. A novel enzyme based biosensor for catechol detection in water samples using artificial neural network. *Biochem. Eng. J.* **2017**, *128*, 1–11.

7. Su, M.; Chen, P.; Dong, Y.; Sun, H. Chemiluminescence of graphene quantum dots induced by acidic potassium permanganate and its application to quenchometric flow-injection assays of hydroquinone in water. *J. Lumin.* **2016**, *177*, 204–208.
8. Jiang, H.; Wang, S.; Deng, W.; Zhang, Y.; Tan, Y. Graphene-like carbon nanosheets as a new electrode material for electrochemical determination of hydroquinone and catechol. *Talanta* **2017**, *164*, 300–306.
9. Deng, M.; Lin, S.; Bo, X.; Guo, L. Simultaneous and sensitive electrochemical detection of dihydroxybenzene isomers with UiO-66 metal-organic framework/mesoporous carbon. *Talanta* **2017**, *174*, 527–538.
10. Lofrano, G.; Rizzo, L.; Grassi, M.; Belgiorno, V. Advanced oxidation of catechol: A comparison among photocatalysis, Fenton and photo-Fenton processes. *Desalination* **2009**, *249*, 878–883.
11. Bukowska, B.; Kowalska, S. Phenol and catechol induce prehemolytic and hemolytic changes in human erythrocytes. *Toxicol. Lett.* **2004**, *152*, 73–84. [CrossRef] [PubMed]
12. Lin, S.H.; Juang, R.S. Adsorption of phenol and its derivatives from water using synthetic resins and low-cost natural adsorbents: A review. *J. Environ. Manag.* **2009**, *90*, 1336–1349.
13. Yin, H.; Zhang, Q.; Zhou, Y.; Ma, Q.; Liu, T.; Zhu, L.; Ai, S. Electrochemical behavior of catechol, resorcinol and hydroquinone at graphene-chitosan composite film modified glassy carbon electrode and their simultaneous determination in water samples. *Electrochim. Acta* **2011**, *56*, 2748–2753. [CrossRef]
14. Tor, A.; Cengeloglu, Y.; Aydin, M.E.; Ersoz, M. Removal of phenol from aqueous phase by using neutralized red mud. *J. Colloid Interface Sci.* **2006**, *300*, 498–503. [CrossRef] [PubMed]
15. Villegas, L.G.C.; Mashhadi, N.; Chen, M.; Mukherjee, D.; Taylor, K.E.; Biswas, N. A Short Review of Techniques for Phenol Removal from Wastewater. *Curr. Pollut. Reports* **2016**, *2*, 157–167.
16. Sulaymon, A.H.; Ahmed, K.W. Competitive adsorption of furfural and phenolic compounds onto activated carbon in fixed bed column. *Environ. Sci. Technol.* **2008**, *42*, 392–397.
17. László, K. Adsorption from aqueous phenol and aniline solutions on activated carbons with different surface chemistry. *Colloids Surf. A Physicochem. Eng. Asp.* **2005**, *265*, 32–39.
18. Kim, S.I.; Yamamoto, T.; Endo, A.; Ohmori, T.; Nakaiwa, M. Adsorption of phenol and reactive dyes from aqueous solution on carbon cryogel microspheres with controlled porous structure. *Microporous Mesoporous Mater.* **2006**, *96*, 191–196.
19. Ania, C.O.; Parra, J.B.; Pis, J.J. Effect of texture and surface chemistry on adsorptive capacities of activated carbons for phenolic compounds removal. *Fuel Process. Technol.* **2002**, *77–78*, 337–343.
20. Roostaei, N.; Tezel, F.H. Removal of phenol from aqueous solutions by adsorption. *J. Environ. Manag.* **2004**, *70*, 157–164. [CrossRef]
21. Pan, B.C.; Meng, F.W.; Chen, X.Q.; Pan, B.J.; Li, X.T.; Zhang, W.M.; Zhang, X.; Chen, J.L.; Zhang, Q.X.; Sun, Y. Application of an effective method in predicting breakthrough curves of fixed-bed adsorption onto resin adsorbent. *J. Hazard. Mater.* **2005**, *124*, 74–80. [CrossRef]
22. Ahmaruzzaman, M.; Sharma, D.K. Adsorption of phenols from wastewater. *J. Colloid Interface Sci.* **2005**, *287*, 14–24. [CrossRef]
23. Wang, H.L.; Jiang, W.F. Adsorption of Dinitro Butyl Phenol (DNBP) from aqueous solutions by fly ash. *Ind. Eng. Chem. Res.* **2007**, *46*, 5405–5411. [CrossRef]
24. Gupta, V.K.; Ali, I.; Saini, V.K. Removal of chlorophenols from wastewater using red mud: An aluminum industry waste. *Environ. Sci. Technol.* **2004**, *38*, 4012–4018. [CrossRef] [PubMed]
25. Jain, A.K.; Gupta, V.K.; Jain, S. Suhas, Removal of Chlorophenols Using Industrial Wastes. *Environ. Sci. Technol.* **2004**, *38*, 1195–1200. [PubMed]
26. Rio, S.; Faur-Brasquet, C.; Le Coq, L.; Le Cloirec, P. Structure characterization and adsorption properties of pyrolyzed sewage sludge. *Environ. Sci. Technol.* **2005**, *39*, 4249–4257. [CrossRef] [PubMed]
27. Rueda-Marquez, J.J.; Levchuk, I.; Ibañez, P.F.; Sillanpää, M. A critical review on application of photocatalysis for toxicity reduction of real wastewaters. *J. Clean. Prod.* **2020**, *258*, 120694. [CrossRef]
28. Ohteni, B. Photocatalysis by inorganic solid materials: Revisiting its definition, concepts, and experimental procedures. *Adv. Inorg. Chem.* **2011**, *63*, 395–430. [CrossRef]
29. Otheni, B. Photocatalysis A to Z—What We Know and What We Don't Know in A Scientific Sense. *J. Photochem. Photobiol. C Photochem. Rev.* **2010**, *11*, 157–178.
30. Herrmann, J.M. Heterogeneous photocatalysis: Fundamentals and applications to the removal of various types of aqueous pollutants. *Catal. Today* **1999**, *53*, 115–129. [CrossRef]
31. Ohtani, B. Titania photocatalysis beyond recombination: A critical review. *Catalysts* **2013**, *3*, 942–953. [CrossRef]

32. Ahmed, S.; Rasul, M.G.; Martens, W.N.; Brown, R.; Hashib, M.A. Heterogeneous photocatalytic degradation of phenols in wastewater: A review on current status and developments. *Desalination* **2010**, *261*, 3–18. [CrossRef]
33. Mesa, J.J.M.; Arias, J.A.G.; Rojas, H.A.; Espinosa, O.E.C. Photocatalytic degradation of Phenol, Catechol and Hydroquinone over Au-ZnO nanomaterials. *Rev. Fac. Ing.* **2020**, *94*, 24–32.
34. Faisal, M.; Abu Tariq, M.; Muneer, M. Photocatalysed degradation of two selected dyes in UV-irradiated aqueous suspensions of titania. *Dye. Pigment.* **2007**, *72*, 233–239. [CrossRef]
35. Haque, M.M.; Muneer, M. TiO_2-mediated photocatalytic degradation of a textile dye derivative, bromothymol blue, in aqueous suspensions. *Dye. Pigment.* **2007**, *75*, 443–448. [CrossRef]
36. Shukla, P.R.; Wang, S.; Ang, H.M.; Tadé, M.O. Photocatalytic oxidation of phenolic compounds using zinc oxide and sulphate radicals under artificial solar light. *Sep. Purif. Technol.* **2010**, *70*, 338–344. [CrossRef]
37. Rafiee, E.; Noori, E.; Zinatizadeh, A.A.; Zanganeh, H. Photocatalytic degradation of phenol using a new developed TiO_2/graphene/heteropoly acid nanocomposite: Synthesis, characterization and process optimization. *RSC Adv.* **2016**, *6*, 96554–96562. [CrossRef]
38. Ma, Y.; Li, Y.; Mao, M.; Hou, J.; Zeng, M.; Zhao, X. Synergetic effect between photocatalysis on TiO_2 and solar light-driven thermocatalysis on MnOx for benzene purification on MnOx/TiO_2 nanocomposites. *J. Mater. Chem. A* **2015**, *3*, 5509–5516. [CrossRef]
39. Chen, Y.; Qian, J.; Wang, N.; Xing, J.; Liu, L. In-situ synthesis of CNT/TiO_2 heterojunction nanocomposite and its efficient photocatalytic degradation of Rhodamine B dye. *Inorg. Chem. Commun.* **2020**, *119*, 108071. [CrossRef]
40. Zhu, Z.; Wang, C.; Liang, L.; Yu, D.; Sun, J.; Zhang, L.; Zhong, S.; Liu, B. Synthesis of Novel Ternary Photocatalyst Ag3PO4/Bi2WO6/Multi-Walled Carbon Nanotubes and Its Enhanced VisibleLight Photoactivity for Photodegradation of Norfloxacin. *J. Nanosci. Nanotechnol.* **2020**, *20*, 2247–2258. [CrossRef]
41. Liu, G.; Liao, M.; Zhang, Z.; Wang, H.; Chen, D.; Feng, Y. Enhanced photodegradation performance of Rhodamine B with g-C3N4 modified by carbon nanotubes. *Sep. Purif. Technol.* **2020**, *244*, 116618. [CrossRef]
42. Su, M.; He, C.; Zhu, L.; Sun, Z.; Shan, C.; Zhang, Q.; Shu, D.; Qiu, R.; Xiong, Y. Enhanced adsorption and photocatalytic activity of BiOI-MWCNT composites towards organic pollutants in aqueous solution. *J. Hazard. Mater.* **2012**, *229–230*, 72–82. [CrossRef]
43. Misra, M.; Chowdhury, S.R.; Lee, T.I. Sunlight driven decomposition of toxic organic compound, coumarin, p-nitrophenol, and photo reduction of Cr(VI) ions, using a bridge structure of Au@CNT@TiO_2 nanocomposite. *Appl. Catal. B Environ.* **2020**, *272*, 118991. [CrossRef]
44. Moya, A.; Barawi, M.; Aleman, B.; Zeller, P.; Amati, M.; Monreal-Bernal, A.; Gregoratti, L.; O'Shea, V.A.D.L.P.; Vilatela, J.J. Interfacial studies in CNT fibre/TiO_2 photoelectrodes for efficient H_2 production. *Appl. Catal. B* **2020**, *268*, 118613. [CrossRef]
45. Colina-Marquez, J.; Machuca-Martinez, F.; Li Puma, G. Radiation Absorption and Optimization of Solar Photocatalytic Reactors for Environmental Applications. *Environ. Sci. Technol.* **2010**, *44*, 5112–5120. [CrossRef] [PubMed]
46. Ustaoglu, A.; Alptekin, M.; Okajima, J.; Maruyama, S. Evaluation of uniformity of solar illumination on the receiver of compound parabolic concentrator (CPC). *Solar Energy* **2016**, *132*, 150–164. [CrossRef]
47. Grčić, I.; Li Puma, G. Six-flux absorption-scattering models for photocatalysis under wide-spectrum irradiation sources in annual and flat reactors using catalysts with different optical properties. *App. Catal. B* **2017**, *211*, 222–234.
48. Grčić, I.; Papić, S.; Brnardić, I. Photocatalytic Activity of TiO_2 Thin Films: Kinetic and Efficiency Study. *Int. J. Chem. React. Eng.* **2017**, *16*, 20160153. [CrossRef]
49. Grčić, I.; Melnjak, I.; Radetić, L.; Premur, V.; Anić Vučinić, A. Predictive Models for Environmental Pollutants Degradation by Solar Photocatalysis in Flat-Plate Reactors. In *New Technologies in Water Sector–Conference Proceedings*; IWA the International Water Association: London, UK, 2018; pp. 317–324.
50. Grčić, I.; Marčec, J.; Radetić, L.; Radovan, A.M.; Melnjak, I.; Jajčinović, I.; Brnardić, I. Ammonia and methane oxidation on TiO_2 supported on glass fiber mesh under artificial solar irradiation. *Environ. Sci. Pollut. Res.* **2020**. [CrossRef]

51. Valencia, S.; Marín, J.M.; Restrepo, G. Study of the bandgap of synthesized titanium dioxide nanoparticles using the sol-gel method and a hydrothermal treatment. *Open Mater. Sci. J.* **2010**, *4*, 9–14. [CrossRef]
52. Turković, A.; Ivanda, M.; Drašner, A.; Vraneša, V.; Peršin, M. Raman spectroscopy of thermally annelaled TiO_2 thin films. *Thin Solid Film.* **1991**, *198*, 199–205. [CrossRef]